

# Geophysical Research Letters<sup>®</sup>

## RESEARCH LETTER

10.1029/2022GL099184

### Key Points:

- The Weifang segment of the Tanlu fault zone shows a noticeable crustal anisotropy with a fast axis parallel to the NNE oriented fault
- East to the fault zone, fast direction rotates rapidly by  $\sim 90^\circ$  to ESE, parallel to the SKS fast polarization direction
- The southeastern part of the study area has a thinned crust with a  $V_p/V_s$  ratio measurably lower than a typical cratonic crust

### Supporting Information:

Supporting Information may be found in the online version of this article.

### Correspondence to:

H. Chen,  
chchao@cup.edu.cn

### Citation:

Miao, W., Niu, F., & Chen, H. (2023). Sharp changes of crustal seismic anisotropy across the central Tanlu fault zone in East China. *Geophysical Research Letters*, 50, e2022GL099184. <https://doi.org/10.1029/2022GL099184>

Received 21 JUN 2022

Accepted 19 DEC 2022

### Author Contributions:

**Conceptualization:** Fenglin Niu, Haichao Chen

**Formal analysis:** Wenpei Miao

**Funding acquisition:** Fenglin Niu, Haichao Chen

**Methodology:** Wenpei Miao, Fenglin Niu

**Project Administration:** Fenglin Niu

**Resources:** Wenpei Miao, Haichao Chen

**Software:** Fenglin Niu

**Visualization:** Fenglin Niu

**Writing – original draft:** Wenpei Miao

**Writing – review & editing:**

Haichao Chen

© 2022. The Authors.

This is an open access article under the terms of the [Creative Commons Attribution-NonCommercial-NoDerivs License](https://creativecommons.org/licenses/by/4.0/), which permits use and distribution in any medium, provided the original work is properly cited, the use is non-commercial and no modifications or adaptations are made.

## Sharp Changes of Crustal Seismic Anisotropy Across the Central Tanlu Fault Zone in East China

Wenpei Miao<sup>1,2</sup>, Fenglin Niu<sup>2,3</sup> , and Haichao Chen<sup>3</sup> 

<sup>1</sup>Institute of Geophysics, China Earthquake Administration, Beijing, China, <sup>2</sup>Department of Earth, Environmental and Planetary Sciences, Rice University, Houston, TX, USA, <sup>3</sup>State Key Laboratory of Petroleum Resources and Prospecting and Unconventional Petroleum Research Institute, China University of Petroleum at Beijing, Beijing, China

**Abstract** Both seismic and geodetic data suggested that the  $\sim 120$ -km long Weifang segment of the Tanlu fault zone, a large-scale active strike-slip system at east China, is a seismic gap with no obvious along-strike shear motion at surface. Measuring crustal deformation around the segment is crucial to constrain stress/strain buildup and potential seismic risk at the fault. We measured crustal and upper mantle seismic anisotropy using P-to-S converted waves at the Moho ( $P_m$ s) and core-mantle boundary (SKS) recorded by broadband arrays across the Weifang fault segment. The measured crustal anisotropy inside the fault zone shows a fast direction of  $\sim$ NNE, parallel to the fault orientation. Right east to the fault zone, the fast axis rotates by almost  $90^\circ$  to ESE. The crustal anisotropy within the fault zone could be caused by aligned microcracks and foliated minerals due to long-lasting shear motion inside the fault zone.

**Plain Language Summary** The Tanlu fault zone (TLFZ) is the most prominent fault system in east China, an area with a large population and economy. One of the most devastating earthquakes in recent history of China, the M8+ Tancheng earthquake occurred in the central segment of this fault. The Weifang segment north to the Tancheng earthquake has little seismicity and is considered as a seismic gap region. Surface Global Positioning System (GPS) data, however, suggested that there is very little present-day crustal deformation across the North China Plain where the Weifang segment is located. This is also supported by shear-wave splitting measurements of the core phases (SKS). Therefore, it is unclear whether the seismic gap is due to lack of strain/stress buildup, or the GPS/SKS data have no resolution on crustal deformation. In this study, we deployed a dense seismic array across the segment, and chose a seismic wave, a P-to-S converted wave at the crust-mantle boundary (i.e., the Moho), to measure crustal deformation. The measured seismic property indicates the presence of aligned microcracks and foliated minerals within the fault zone, which suggests significant shear deformation is occurring inside the TLFZ.

## 1. Introduction

The NNE-trending Tanlu fault zone (TLFZ) located at east China is a large-scale strike-slip system that extends from the Qinling-Dabie Orogenic Belt in the south to the Xing-Meong block (Amurian Block) in the north with a total length of  $\sim 2,400$  km within China (Figure 1). The fault zone runs across the North China Block (NCB) and has been proposed to be formed from the collision of the NCB and the South China Block (SCB) in middle Triassic times (e.g., Yin & Nie, 1993). The fault zone is active and capable of producing M8+ earthquakes (e.g., Zhang et al., 2018; Zhu et al., 2018), which could cause tremendous life loss and property damage, as the fault zone is surrounded by highly populated areas. Monitoring the deformation and seismicity of the fault zone thus is highly important for seismic hazard mitigation.

Zhu et al. (2018) relocated earthquakes with a magnitude less than M5 occurring on the central section of the fault zone between 1990 and 2014 using the double-difference location method. The section is located inside the Shandong province and extends between  $\sim 34^\circ$ N and  $\sim 37^\circ$ N. It is believed to be the segment where the M7 Anqiu earthquake and M8+ Tancheng earthquake occurred around 70 B.C. and in 1,668, respectively (Figure 1). The current seismicity appears to occur mainly along the rupture zone of the Tancheng earthquake (hereinafter referred to as the Tancheng segment) while the section north to the Anqiu earthquake (Weifang segment) seems to lack microseismic activity (Zhu et al., 2018), that is, a seismic gap. The Weifang segment is composed of several surface fault traces separated by a few to tens of kilometers (Figure 1b).

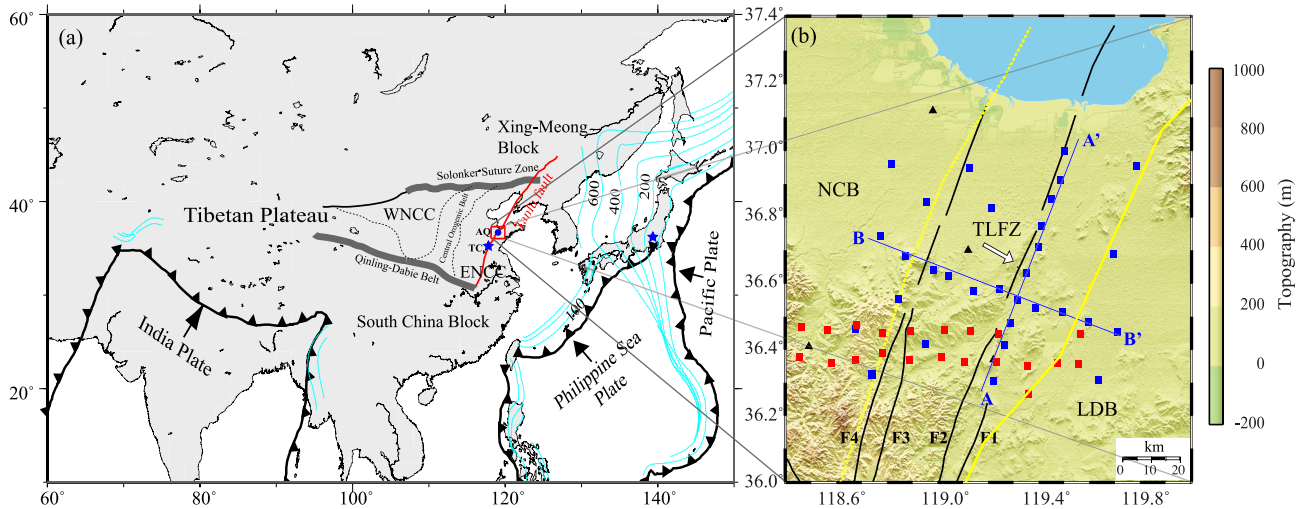


**Figure 1.** (a) Map showing the location of the Tanlu fault (red line) and tectonic settings around the fault. Arrows indicate the subduction of the Pacific and Philippine plates, and the collision of the Indian plate at the east and southwest sides of China, respectively. Cyan lines indicate the descending Pacific, Philippine, and Indian plates. The thick gray lines outline the Qinling-Dabie orogenic belt and the Solonker Suture Zone. ENCC and WNCC are the eastern and western North China Craton bounded by the Central Orogenic Belt. TC (TanCheng) and AQ (AnQiu) represent the 1668 M8+ Tancheng earthquake and the 70 B.C. M7 Anqiu earthquake, respectively. Red box indicates the study area. (b) Topographic map showing the Tanlu fault zone (TLFZ). Black solid lines indicate the four surface traces (F1, F2, F3, and F4) of the TLFZ. The dotted and solid yellow lines indicate the western and eastern boundaries of the TLFZ that separates the North China Block from the Ludong block. Blue and red squares show the broadband stations of the TLarray and the NCISarray, respectively. Black triangles indicate the permanent seismic stations of the China Earthquake Administration. The open white arrow shows the absolute plate motion direction of the Eurasia plate of HS3-NUVEL1A. The blue line BB' indicate the Moho depth profile shown Supporting Information S1 (Figure S10).

Many studies suggested that the TLFZ started with a sinistral motion in early Paleozoic and changed to normal faulting in early Cretaceous (Zhu et al., 2010). Since Quaternary the motions along the fault zone are mainly dextral with a minor component of thrust (Zhu et al., 2015). The dextral motion is, however, less obvious on the present-day Global Positioning System (GPS) data measured at the North China Plain (NCP), which shows a motion direction of N100°–120°E (Zhang et al., 2018). The along-strike shear deformation is also not suggested by seismic anisotropy data measured from SKS splitting. The fast polarization directions measured from stations in NCP (Chang et al., 2009) are mainly WNW-ESE, which is roughly parallel to the GPS and absolute plate motion (APM) direction of ~N118.2°E (Gripp & Gordon, 2002), but perpendicular to the strike of the TLFZ. The SKS and GPS observations may suggest that there is little to no simple-shear deformation within the fault zone and the observed seismicity gap is due to lack of stress/strain build up. An alternative explanation is that the deformation occurs mainly inside the crust, which is unresolvable by the SKS data as its crustal raypath is much shorter than the mantle path.

Recent surface wave studies (Bem et al., 2022; Luo & Yao, 2021) indicated that azimuthal anisotropy in the crust beneath the southern segments of the Tanlu fault has a fast propagation direction parallel to the fault, suggesting a different deformation pattern between the crust and underneath mantle lithosphere around the fault. In theory, it is difficult to measure azimuthal anisotropy using surface waves propagating in different directions because of the tradeoff between anisotropy and heterogeneities along raypaths. This tradeoff, however, disappears in the case of polarization anisotropy, where velocity of seismic waves traveling along a similar raypath varies with its polarization directions, leading to the so-called shear-wave splitting. Using P-to-S converted wave at the Moho, Pms, Zheng et al. (2019) observed a fault-parallel anisotropy in the crust of the Zhangjiakou-Penglai Fault Zone in north China. Xu et al. (2021) measured crustal anisotropy from teleseismic records of a dense seismic array across the Trans-North China Orogen and found that the fast polarization directions of nearly vertically propagating S waves are roughly parallel to the strikes of faults and mountain ranges in the study area.

To better constrain seismic structure of the shear zone and to better monitor local seismic activity in the gap region, we deployed a dense array with 31 broadband sensors across the Weifang segment of the TLFZ between August of 2017 and July of 2018. We employed the Pms wave to measure crustal anisotropy using a common conversion gathering method. We also measured shear wave splitting of the P-to-S converted wave at the core-mantle boundary (CMB), SKS, to constrain seismic anisotropy of the upper mantle. The measured crustal

and mantle seismic anisotropy are used to constrain mechanisms of deformation and flows occurring in the crust, mantle lithosphere, and asthenosphere.

## 2. Data

In this study, we used waveform data of a temporary dense broadband array installed across the Weifang segment of the Tanlu Fault (hereinafter referred to as TLarray). The array was deployed between August of 2017 and July of 2018 and comprised 31 Nanometrics trillium 120 posthole sensors and centaur digitizers with a station spacing of  $\sim 5\text{--}30$  km (Wang et al., 2021). We also used data from another linear array with 51 broadband stations in the southern part of the study area. The linear array was deployed by the Northern China Interior Structure Project (NCISP) between January of 2000 and October of 2001 (Chen et al., 2006). In the rest of the paper, we refer to it as the NCISPararray. We selected a total of 4,929 receiver functions from 257 M5.5+ events that fall in the distance range of  $30^\circ\text{--}90^\circ$  to investigate azimuthal anisotropy in the crust (Figure S1a in Supporting Information S1). The backazimuthal distribution of the events is shown in Supporting Information S1 (Figure S1b). Specifically, our data cover 11 of the  $30^\circ$ -bins except for the  $0^\circ\text{--}30^\circ$  bin if we divide the full  $360^\circ$ -backazimuth into twelve  $30^\circ$ -bins. For comparison, we also analyzed SKS waveform splitting of two teleseismic events (Table S1 in Supporting Information S1) to estimate azimuthal anisotropy in the upper mantle.

## 3. Method

### 3.1. Estimate Crustal Anisotropy From Pms

We basically followed the procedure of Sun et al. (2012) to estimate crustal anisotropy from the *Pms* phase of radial (*R*) and transverse (*T*) receiver function (RF) data, which includes a harmonic analysis of *Pms* arrival times on *R* component and a joint fitting of the *R*- and *T*-component *Pms* waveforms. The only difference is that the analyses were applied to RFs with a common conversion point (CCP) at 31.0 km, the areal average Moho depth of the CRUST 1.0 model (Laske et al., 2013), instead of RFs gathered at individual stations. This can significantly increase the number of RFs at each grid in a dense-array setting.

Since *Pms* on RFs is a normalized phase, that is, a Green's function from an impulse source, we can apply stacking analysis using *Pms* phases from different earthquakes. To generate RFs, we first rotated the two horizontal components to the *R* and *T* components. We then approximated the vertical (*Z*) component as the earthquake source time function and deconvolved it from the corresponding *R* and *T* components recordings, which are referred to as the *R*- and *T*-component RFs, respectively. We employed a frequency-domain deconvolution using the water-level technique (Clayton & Wiggins, 1976) and a Gaussian lowpass filter. The wave-level and corner frequency were set to 0.01 and 0.5 Hz, respectively. These parameters were chosen to obtain high-quality RFs (Table S2, Figure S2 in Supporting Information S1). We manually checked all receiver functions and selected a total of 4,929 pairs of *R* and *T* receiver functions that show a signal-to-noise ratio (SNR)  $\geq 3$ . The SNR is defined as the ratio of signal amplitude to the noise amplitude.

Based on the source-receiver geometry, we first computed the geographic locations of the P-to-S conversion points at 31 km depth by ray tracing the IASP91 model (Kennett & Engdahl, 1991). We then divided study area ( $36.3^\circ\text{--}37.0^\circ\text{N}$ ,  $118.5^\circ\text{--}119.8^\circ\text{E}$ ) into meshed grids of  $0.05^\circ$  by  $0.05^\circ$  and used a circular cap with a radius of  $0.1^\circ$  to gather RFs. This is based on the fact that *Pms* conversion points are located  $\sim 0.1^\circ$  away from the receiver. For each meshed grid with more than 40 receiver functions, we first conducted *H*- $\kappa$  stacking analysis to determine Moho depth (*H*) and average *Vp/Vs* ratio ( $\kappa$ ). We employed a refined *H*- $\kappa$  stacking method (Niu et al., 2007), which introduces a coherence function among the *Pms* and the two multiples in the stacking to reduce the tradeoff between Moho depth and *Vp/Vs* ratio. Figure S3 in Supporting Information S1 shows the *H*- $\kappa$  stacking results at grids *C* ( $119.75^\circ\text{E}$ ,  $36.50^\circ\text{N}$ ), *D* ( $119.75^\circ\text{E}$ ,  $36.45^\circ\text{N}$ ), *E* ( $118.45^\circ\text{E}$ ,  $36.70^\circ\text{N}$ ), and *F* ( $118.80^\circ\text{E}$ ,  $36.60^\circ\text{N}$ ). The latter two are from the northwest region with high *Vp/Vs* ratios.

It should be noted that the CCP-based method implies a smoothing over a circular area ( $0.2^\circ$  in radius), approximately three times larger than that ( $0.1^\circ$  in radius) of the single-station method. Figure S4 in Supporting Information S1 shows the sampling volumes of RFs gathered at a receiver (a cone shaded in cyan) and a CCP cap (a reversed frustum of cone shaded in gray), respectively. The benefit of the CCP method is a significant increase in the number of RFs, for example, the most sampled grid has 764 RFs while the maximum number of RFs recorded

at a station is 111. Figure S5 in Supporting Information S1 shows  $H$ - $\kappa$  results of single-station and CCP-based stacking, respectively. The large number of RFs is an advantage to raise the SNR of RFs in each azimuthal bin, which is the key parameter that controls the measurement precision of crustal anisotropy.

Since the  $P$ ms arrival has a negative distance moveout with respect to the direct  $P$  wave, we used the  $H$ - $k$  results to compute the moveout and make a time correction to align all the  $P$ ms arrivals at the relative time corresponding to an epicentral distance of  $60^\circ$  and a source depth of 0 km. We further normalized the  $R$ - and  $T$ -RFs by dividing them by the peak amplitude of the  $P$  wave on the  $R$  component. We finally applied the harmonic analysis and joint inversions of crustal anisotropy using the preprocessed RFs.

When  $P$ ms travels through an anisotropic crust with a horizontally symmetrical axis, its arrival time is expected to show a cosine variation in the backazimuthal direction ( $\theta$ ) with a period of  $180^\circ$  ( $\cos 2\theta$ ). Also, it can be shown that the  $T$ -RFs are proportional to the time derivatives of the  $R$ -RFs with a  $\cos 2\theta$  variation in amplitude (Liu & Niu, 2012). We utilized these two unique features of  $P$ ms to robustly extract fast polarization direction ( $\varphi_c$ ) and delay time ( $\delta t_c$ ). The method included searches for  $(\varphi_c, \delta t_c)$  based on three individual objective functions (IOFs) and one joint objective function (JOF), as well as analyses on measurement robustness. The three IOFs are: (a) the peak energy of the stacked  $R$ -RF after a cosine moveout correction in the  $P$ ms arrival time; (b) the cross-correlation of the  $R$ -RFs after a full correction of crustal anisotropy; (c) the total energy of stacked  $T$ -RF after a removal of crustal anisotropy. The JOF was computed by taking the product of the first two IOFs and a further division of the third IOF. The robustness analyses include a harmonic analysis and statistical tests based on the principle that stacking a total of  $N$  coherent signals can lead to an increase of SNR by a factor of  $N^{1/2}$ . Further details on the method can be found in Liu and Niu (2012) and Sun et al. (2012).

### 3.2. Estimate Mantle Anisotropy From SKS

SKS splitting is not the main new data as it has been measured by many previous studies (e.g., Chang et al., 2009). Our main goal here is to make precise splitting measurements with high SNR ( $>5$ ) SKS data. Since there are only two earthquakes and their backazimuths are  $\sim 90^\circ$  apart (Table S1 in Supporting Information S1), we can combine the data from the two earthquakes and search for a pair of  $(\varphi_m, \delta t_m)$  that minimizes either the summed energy in the  $T$ -component or the summed second eigenvalue of the covariance matrix of the corrected particle motion (Li & Niu, 2010). The SNR of the horizontal components are used as the weight between the two events. We vary  $\varphi_m$  in the range of  $0^\circ$ – $180^\circ$  with an increment of  $1^\circ$ , and  $\delta t_m$  from 0.0 to 4.0 s in increments of 0.01 s in the 2-D grid search.

## 4. Results

### 4.1. Moho Depth and $V_p/V_s$ Ratio

As shown in Supporting Information S1 (Figure S3), we were able to find the global maxima in the  $H$ - $\kappa$  domain at most of the grid points due to large number of RFs gathered at each grid. Since a circular bin of  $0.1^\circ$  is used in the stacking, measurement at each grid should be considered as the averaged value over the circular area. Figures 2a and 2b show the measured Moho depth and  $V_p/V_s$  ratio, respectively. Moho depth varies from 31.0 to 36.8 km with an average of 33.3 km, and  $V_p/V_s$  ratio varies from 1.648 to 1.861 with an average of 1.736. In general, the eastern part of the study area has a slightly deeper Moho and a lower  $V_p/V_s$  (blue regions in Figure 2).

### 4.2. Crustal Anisotropy

Figure 3 shows the two measurements of crustal anisotropy at two grids: one inside the TLFZ (a) and the other one in the Ludong block (LDB, b). The raw  $R$ -RFs are shown in Supporting Information S1 (Figure S6). Here we only showed the  $(\varphi_c, \delta t_c)$  results from the joint inversion. In addition to the regular  $0.05^\circ$  by  $0.05^\circ$  grids, we also made measurements along the two dense deployment lines, AA' and BB' (Figure 1b). We only selected those grids that exhibit a strong degree-2 azimuthal variation and pass the SNR statistical tests. We obtained a total of 81 robust measurements of  $(\varphi_c, \delta t_c)$ , which are shown in Figure 4a. The  $(\varphi_c, \delta t_c)$  values here are estimated from the JOF. Figure 4a indicates that crust in the study area exhibits a noticeable azimuthal anisotropy. The splitting time varies from 0.07 to 0.41 s with an average of 0.22 s, which is equivalent to a seismic anisotropy of 0.8%–4.6% and an average of 2.4% if we use an S-wave traveltime of  $\sim 9.0$  s inside the crust, assuming a crust

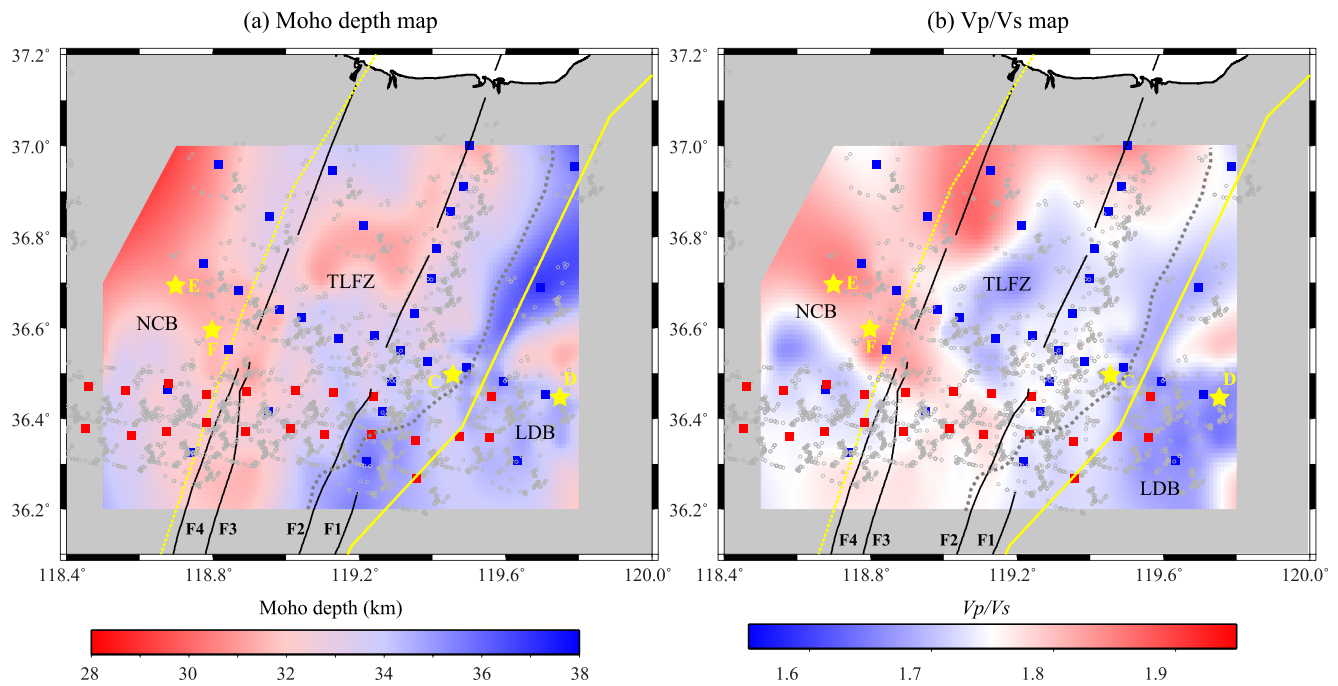


**Figure 2.** Maps showing variations of (a) Moho depth and (b)  $V_p/V_s$  ratio of the study area. Symbols and abbreviations are the same as Figure 1b. The yellow stars labeled as C, D, E, and F indicate the four grids whose H- $\kappa$  stacking results are shown in Supporting Information S1 (Figure S3). The schematically drawn dotted gray line outlines the boundary of rapid changes in Moho depth. For grids with no measurements, we employed an interpolation to fit a flattest Moho (or  $V_p/V_s$  ratio) based on a regularized inversion (Niu et al., 2007).

with a thickness of 33.3 km, a  $V_p/V_s$  ratio of 1.736, and a  $V_p$  of 6.4 km/s. The fast polarization direction of  $P_{ms}$  shows a consistent N-S to NNE-SSW direction inside the TLFZ, roughly parallel to the strike of the TLFZ. By contrast, the fast direction changes rapidly to WNW-ESE across the eastern edge of the fault zone (solid yellow line in Figure 4a), that is, inside the LDB. The direction is almost the same as the GPS, APM, and the fast SKS direction shown in the next section.

### 4.3. Upper Mantle Anisotropy

We found clear arrivals of SKS with a  $SNR \geq 5$  from two intermediate depth earthquakes that occurred in the central America and Tonga subduction zones, respectively (Table S1 in Supporting Information S1). The SKS arrivals have significant energy on the transverse component (Figure S7 in Supporting Information S1) with an elliptical particle motion (Figure S8 in Supporting Information S1), indicating that SKS propagates through an anisotropic medium after the P-to-S conversion at the CMB. We searched for two sets of  $(\varphi_m, \delta t_m)$  that minimize the summed  $T$ -energy and the summed second eigenvalue of the horizontal 2-D covariance matrix. An example of the 2-D grid searches at station TL. AA05 is shown in Supporting Information S1 (Figure S9). The resulting  $(\varphi_m, \delta t_m)$  from the two methods are consistent with each other, suggesting that the transverse energy of SKS is mainly caused by waveform splitting through an anisotropic medium. We obtain  $(\varphi_m, \delta t_m)$  at 28 stations, which are shown in Figure 4b. The SKS splitting parameters observed here are generally consistent with those reported by Chang et al. (2009). A large portion of the stations show a fast polarization direction of WNW-ESE, which lies roughly in the direction of APM and surface GPS motion. The observed splitting time varies from 0.70 to 1.96 s with an average of  $1.18 \pm 0.22$  s. Stations located inside the LDB (yellow circles) generally show a larger splitting time ( $1.49 \pm 0.32$  s) with a fast polarization azimuth more aligned with the APM direction (Figure 4b). Conversely, stations inside the TLFZ and the NCB have a slightly smaller delay time ( $1.10 \pm 0.16$  s) and a fast polarization azimuth slightly different from the APM direction.

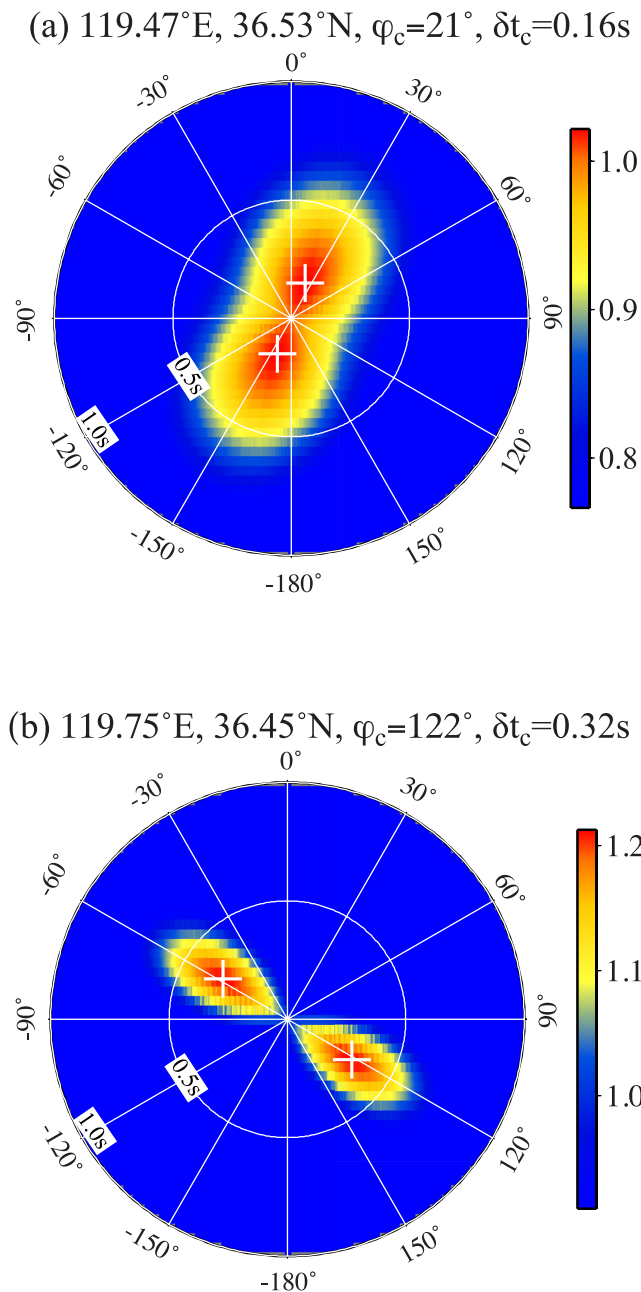


**Figure 3.** Measurement examples of crustal anisotropy from two locations inside (a) and outside (b) the Tanlu fault zone. The joint objective function of stacked  $R$ -RF energy,  $R$ -RFs cross correlation, and  $T$ -RF energy is shown as a function of fast polarization direction ( $\varphi_c$ ) and splitting time ( $\delta t_c$ ). The two circles represent  $\delta t_c = 0.5$  and  $1.0$  s, respectively.

## 5. Discussion

The San Andreas fault between the Pacific plate and the North America plate is featured as a Moho step with a depth difference of  $\sim 8$ – $10$  km (Henstock et al., 1997; L. Zhu, 2002), suggesting that the fault cuts through the entire crust. The TLFZ is generally thought to be suture zone between the NCB and SCB (e.g., Yin & Nie, 1993), although there are several hypotheses on its tectonic origin (Xu & Zhu, 1994). Our results show a change of  $\sim 2$ – $4$  km in Moho depth across a schematic boundary (dashed gray line in Figure 2) in the eastern part of the fault zone, which might suggest that the eastern fault branches are likely to penetrate deeply and cut through the entire crust. However, since the total uncertainties in estimating Moho depth are likely to be  $\sim 2$ – $3$  km, therefore, it is still difficult to conclude that such a step does exist across the boundary. Chen et al. (2006) migrated RFs recorded by the NCISPararray (red squares in Figure 2) and obtained an image of Moho and the lithosphere-asthenosphere boundary (LAB) along an E-W profile at a latitude of  $\sim 36.4^{\circ}\text{N}$ . They found a  $\sim 4$  km uplift of the Moho beneath the TLFZ and a dome shaped LAB at a depth of 60- to 80-km beneath the profile. We also observed an uplift of Moho beneath the BB' profile from our common-converted point image of RF data when the 1D IASP91 model was used as the reference model (Figure S10a in Supporting Information S1). However, if we employ the  $V_p/V_s$  ratio measured by the  $H$ - $k$  analysis and jointly migrate the  $P$ ms and the two multiples, the imaged Moho shows much less depth variations across the profile (Figure S10b in Supporting Information S1). Since the western end of the profile has a thick sedimentary layer (e.g., Yang & Badal, 2013), its high  $V_p/V_s$  ratio could lead to an overestimate of Moho depth if a regular  $V_p/V_s$  ratio is employed in the migration.

The average  $V_p/V_s$  ratio over the southeast part of the study area outlined by the dashed gray line is  $1.693 \pm 0.023$ , which is measurably lower than the average  $V_p/V_s$  ratio of 1.766 estimated by Christensen (1996). Niu and James (2002) obtained a moderate  $V_p/V_s$  ratio of  $1.742 \pm 0.007$  at the Archean Kaapvaal craton. The low  $V_p/V_s$  ratio here suggests that the crust in the southeast part of the study is more felsic in composition than a regular Archean crust, which is consistent with a scenario that part of the Archean lower crust was delaminated during the destruction of North China Craton in the early Cretaceous (e.g., Menzies et al., 1993).

The  $P$ ms data showed an average splitting time of 0.22 s along its  $\sim 9$  s travel path of the crust (Figure 4a). For comparison, Audet (2015) measured crustal anisotropy using RF data recorded by a broadband array across the Parkfield section of the San Andreas Fault in western US and found that the fast direction is parallel to the NW-SE oriented strike of the fault. He further suggests that the observed azimuthal anisotropy is sourced in a 5–10 km thick layer in the upper crust due to aligned fluid-filled microcracks, and the width of the anisotropic zone extends to  $>3$  km away from the surface fault trace, much wider than the 100–300 m of low-velocity damage zone. It is conceivable that the observed azimuthal anisotropy inside the TLFZ comes from the shallow part of the crust filled with microcracks that aligned along the shear

direction. However, it is also possible that the observed crustal anisotropy is caused by foliated mica shists or other minerals in the middle and lower crust. Other types of data, such as directional dependent Rayleigh wave phase velocity (e.g., Liu et al., 2019) and polarization (Zhang et al., 2020) data measured from ambient noise Green's functions, could further constrain the depth distribution of seismic anisotropy inside the crust.

We notice that crustal anisotropy changes rapidly across the eastern boundary of the TLFZ (solid yellow line in Figure 4a). Beneath the LDB, the fast polarization direction inside the crust appears to align with the SKS fast

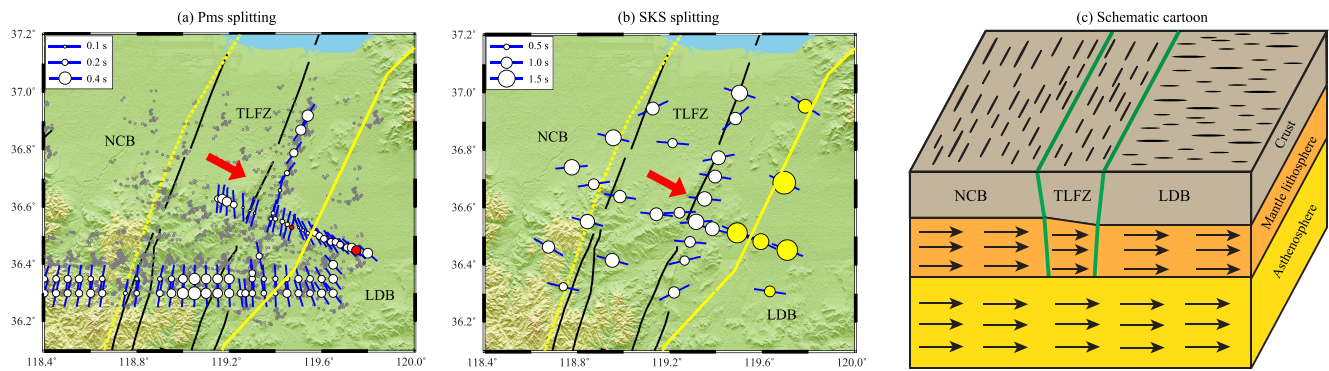


**Figure 4.** Maps showing the fast direction and splitting time of (a) *Pms* and (b) SKS. Symbols and abbreviations are the same as Figure 1b. The fast-axis direction is shown by a blue line and the amount of splitting time is indicated by the size of circle plotted at the measurement location. The red arrow indicates the absolute plate motion direction. (a) Note there is a rapid change in fast polarization direction of *Pms* across the eastern edge of the fault zone. (b) The SKS fast polarization directions measured at all the stations show an ESE-WNW direction. Stations on the Ludong block are shown in yellow circles. (c) Schematic representation of crustal and mantle deformation within the Tanlu fault zone and its surrounding blocks.

direction, and the SKS splitting times are slightly larger than those in the west (Figure 4b). Figure 4c shows a cartoon illustrating crustal deformation and mantle flow based on *Pms* and SKS data. Since SKS splitting reflects the integrated effects of the upper mantle and the crust, the above observations suggest that mantle and crust beneath LDB share the same fast direction and therefore their splitting times can be constructively summed, leading to a large SKS splitting time. Our observations here thus imply that the entire lithosphere of the LDB has been deformed coherently in the vertical direction.

The SKS fast polarization directions here are consistent with those of Chang et al. (2009), which are dominantly ESE-WNW (Figure 4b). They are almost perpendicular to the fast direction of the crustal anisotropy within the TLFZ and NCB. This is consistent with recent surface wave studies of the southern part of the TLFZ, where the crust and upper mantle also have different deformation patterns (Bem et al., 2022; Luo & Yao, 2021). In addition, such a discrepancy was also seen in western US, where SKS data show a near E-W fast direction largely attributed to asthenospheric flow (Silver & Holt, 2002), while *Pms* data near the San Andreas Fault exhibit a fault parallel NW-SE direction (Audet, 2015). In western US, asthenospheric mantle flow direction appears to be different from surface GPS motion direction, which was attributed to deformation within the lithosphere. In our study area, mantle flow direction aligns with surface GPS motion directions, suggesting deformation in the lithosphere is either pure shear or insignificant after it was frozen. Moreover, it is conceivable that the contemporary mantle lithosphere is cooled from asthenosphere after the old cratonic lithosphere was delaminated during the destruction. Therefore, the observed SKS splitting could be partly caused by fossilized fabric of the mantle lithosphere that aligns with the asthenospheric flow.

## 6. Conclusions

We measured crustal anisotropy of the Weifang segment of the TLFZ using a large number of *Pms* data recorded by two dense broadband arrays installed in an area of ~100 km by 80 km across the fault zone. We gathered *Pms* based on the Moho conversion points and employed a joint inversion method to search for a pair of ( $\varphi_c, \delta t_c$ ) that best explained the backazimuthal variations of *Pms* arrival time and polarity on the radial and transverse components, respectively. We found that the crustal anisotropy within the fault zone has a fast direction parallel to the fault strike with an average splitting time of ~0.22 s. We speculate that the observed crustal anisotropy is caused by alignment of fluid-fill microcracks in the upper crust or mineral foliated mica shists or other minerals in the middle and lower crust, due to long-lasting shear motion within the fault zone. Crustal anisotropy shows a sharp change in the fast axis direction across the eastern boundary of the fault zone. Mantle anisotropy measured from SKS splitting data indicates a fast wave speed direction parallel to the APM and surface GPS direction across the entire study area. The relatively large SKS splitting times suggest that both asthenospheric flow and the frozen flow fabric within the thermal lithosphere could be the contributing sources. We also found that the study area is underlain by a thinned crust with a  $V_p/V_s$  ratio measurably lower than a typical cratonic crust,

implying that part of the lower crust has been delaminated during the destruction of North China Craton in early Cretaceous.

## Data Availability Statement

The receiver function waveforms and crustal model in this study are available at <https://doi.org/10.5281/zenodo.6348223>.

## Acknowledgments

We thank all the people involved in the TLarray and NCISP projects for providing the seismic data used in this study. We are grateful to the editor and three anonymous reviewers for their critical review and constructive comments, which significantly improved the quality of this paper. This study was jointly supported by the National Key Research and Development Program of China (No. 2017YFC1500300) and the National Natural Science Foundation of China (No. 41974045 and 42222402).

## References

- Audet, P. (2015). Layered crustal anisotropy around the San Andreas Fault near Parkfield, California. *Journal of Geophysical Research: Solid Earth*, 120(5), 3527–3543. <https://doi.org/10.1002/2014JB011821>
- Bem, T. S., Liu, C., Yao, H., Luo, S., Yang, Y., & Liu, B. (2022). Azimuthally anisotropic structure in the crust and uppermost mantle in central east China and its significance to regional deformation around the Tan-Lu fault zone. *Journal of Geophysical Research: Solid Earth*, 127(3), e2021JB023532. <https://doi.org/10.1029/2021jb023532>
- Chang, L., Wang, C., & Ding, Z. (2009). Seismic anisotropy of upper mantle in eastern China. *Science in China—Series D: Earth Sciences*, 52(6), 774–783. <https://doi.org/10.1007/s11430-009-0073-4>
- Chen, L., Zheng, T., & Xu, W. (2006). A thinned lithospheric image of the Tanlu Fault Zone, eastern China: Constructed from wave equation-based receiver function migration. *Journal of Geophysical Research*, 111(B9), B09312. <https://doi.org/10.1029/2005JB003974>
- Christensen, N. I. (1996). Poisson's ratio and crustal seismology. *Journal of Geophysical Research*, 101(B2), 3139–3156. <https://doi.org/10.1029/95JB03446>
- Clayton, R. W., & Wiggins, R. A. (1976). Source shape estimation and deconvolution of teleseismic bodywaves. *Geophysical Journal International*, 47(1), 151–177. <https://doi.org/10.1111/j.1365-246X.1976.tb01267.x>
- Gripp, A. E., & Gordon, R. G. (2002). Young tracks of hotspots and current plate velocities. *Geophysical Journal International*, 150(2), 321–361. <https://doi.org/10.1046/j.1365-246X.2002.01627.x>
- Henstock, T. J., Levander, A., & Hole, J. A. (1997). Deformation in the lower crust of the San Andreas Fault System in northern California. *Science*, 278(5338), 650–653. <https://doi.org/10.1126/science.278.5338.650>
- Kennett, B. L. N., & Engdahl, E. R. (1991). Traveltimes for global earthquake location and phase identification. *Geophysical Journal International*, 105(2), 429–465. <https://doi.org/10.1111/j.1365-246X.1991.tb06724.x>
- Laske, G., Masters, G., Ma, Z., Pasyanos, M. E., & Livermore, L. (2013). Update on CRUST1.0: A 1-degree global model of Earth's crust. *Geophysical Research Abstracts*, 15. Abstract EGU2013–2658.
- Li, J., & Niu, F. (2010). Seismic anisotropy and mantle flow beneath northeast China inferred from regional seismic networks. *Journal of Geophysical Research*, 115(B12), B12327. <https://doi.org/10.1029/2010JB007470>
- Liu, C., Yao, H., Yang, H., Shen, W., Fang, H., Hu, S., & Qiao, L. (2019). Direct inversion for three-dimensional shear wave speed azimuthal anisotropy based on surface wave ray tracing: Methodology and application to Yunnan, southwest China. *Journal of Geophysical Research: Solid Earth*, 124(11), 11394–11413. <https://doi.org/10.1029/2018JB016920>
- Liu, H., & Niu, F. (2012). Estimating crustal seismic anisotropy with a joint analysis of radial and transverse receiver function data: Estimating crustal seismic anisotropy. *Geophysical Journal International*, 188(1), 144–164. <https://doi.org/10.1111/j.1365-246X.2011.05249.x>
- Luo, S., & Yao, H. (2021). Multistage tectonic evolution of the Tanlu fault: Insights from upper crustal azimuthal anisotropy of the Chao Lake segment. *Tectonophysics*, 806, 228795. <https://doi.org/10.1016/j.tecto.2021.228795>
- Menzies, M. A., Fan, W., & Zhang, M. (1993). Palaeozoic and Cenozoic lithoprobes and the loss of >120 km of Archaean lithosphere, Sino-Korean craton, China. *Geological Society, London, Special Publications*, 76(1), 71–81. <https://doi.org/10.1144/GSL.SP.1993.076.01.04>
- Niu, F., Bravo, T., Pavlis, G., Vernon, F., Rendon, H., Bezada, M., & Levander, A. (2007). Receiver function study of the crustal structure of the southeastern Caribbean plate boundary and Venezuela. *Journal of Geophysical Research*, 112(B11), B11308. <https://doi.org/10.1029/2006JB004802>
- Niu, F., & James, D. E. (2002). Fine structure of the lowermost crust beneath the Kaapvaal craton and its implications for crustal formation and evolution. *Earth and Planetary Science Letters*, 200(1–2), 121–130. [https://doi.org/10.1016/S0012-821X\(02\)00584-8](https://doi.org/10.1016/S0012-821X(02)00584-8)
- Silver, P. G., & Holt, W. E. (2002). The mantle flow field beneath western North America. *Science*, 295(5557), 1054–1057. <https://doi.org/10.1126/science.1066878>
- Sun, Y., Niu, F., Liu, H., Chen, Y., & Liu, J. (2012). Crustal structure and deformation of the SE Tibetan plateau revealed by receiver function data. *Earth and Planetary Science Letters*, 349(350), 186–197. <https://doi.org/10.1016/j.epsl.2012.07.007>
- Wang, Z., Niu, F., Huang, J., Li, Z., & Chen, H. (2021). Distribution of Rayleigh wave microseisms constrained by multiple seismic arrays. *Journal of Geophysical Research: Solid Earth*, 126(9), e2021JB022084. <https://doi.org/10.1029/2021JB022084>
- Xu, J., & Zhu, G. (1994). Tectonic models of the Tan-Lu fault zone, eastern China. *International Geology Review*, 36(8), 771–784. <https://doi.org/10.1080/00206819409465487>
- Xu, X., Ding, Z., Li, L., & Niu, F. (2021). Crustal anisotropy beneath the Trans-North China Orogen and its adjacent areas from receiver functions. *Frontiers of Earth Science*, 9, 753612. <https://doi.org/10.3389/feart.2021.753612>
- Yang, L., & Badal, J. (2013). Mirror symmetry of the crust in the oil/gas region of Shengli, China. *Journal of Asian Earth Sciences*, 78, 327–344.
- Yin, A., & Nie, S. (1993). An indentation model for the North and South China collision and the development of the Tan-Lu and Honam Fault Systems, eastern Asia. *Tectonics*, 12(4), 801–813. <https://doi.org/10.1029/93TC00313>
- Zhang, Y., Niu, F., Tao, K., Ning, J., Chen, H., & Tang, Y. (2020). Hydraulic injection-induced velocity changes revealed by surface wave coda and polarization data at a shale play site in southwest China. *Journal of Geophysical Research: Solid Earth*, 125(10), e2019JB019169. <https://doi.org/10.1029/2019JB019169>
- Zhang, Y. G., Zheng, W. J., Wang, Y. J., Zhang, D. L., Tian, Y. T., Wang, M., et al. (2018). Contemporary deformation of the North China plain from global positioning system data. *Geophysical Research Letters*, 45(4), 1851–1859. <https://doi.org/10.1002/2017GL076599>
- Zheng, T., Ding, Z., Ning, J., Liu, K. H., Gao, S. S., Chang, L., et al. (2019). Crustal azimuthal anisotropy beneath the central North China Craton revealed by receiver functions. *Geochemistry, Geophysics, Geosystems*, 20, 2235–2251. <https://doi.org/10.1029/2019GC008181>

- Zhu, A., Xu, X., Wang, P., Ren, Y., & Sun, D. (2018). The present activity of the central and southern segments of the Tancheng-Lujiang fault zone evidenced from relocated microseismicity and focal mechanisms (in Chinese). *Earth Science Frontiers*, 25(1), 218–226. <https://doi.org/10.13745/j.esf.yx.2016-11-54>
- Zhu, G., Hu, W., Song, L., & Liu, B. (2015). Quaternary activity along the Tan-Lu fault zone in the Bohai Bay, East China: Evidence from seismic profiles. *Journal of Asian Earth Sciences*, 114, 5–17. <https://doi.org/10.1016/j.jseaes.2015.03.030>
- Zhu, G., Niu, M., Xie, C., & Wang, Y. (2010). Sinistral to normal faulting along the Tan-Lu Fault Zone: Evidence for geodynamic switching of the East China continental margin. *The Journal of Geology*, 118(3), 277–293. <https://doi.org/10.1086/651540>
- Zhu, L. (2002). Deformation in the lower crust and downward extent of the San Andreas Fault as revealed by teleseismic waveforms. *Earth Planets and Space*, 54(11), 1005–1010. <https://doi.org/10.1186/BF03353293>